Magneto-electrochemical ammonia synthesis: Boosting nitrite reduction activity by the optimized magnetic field induced in spin polarized system

Ashadul Adalder[1], Koushik Mitra[1], Narad Barman[2], Ranjit Thapa[2], Sourav Bhowmick[1], Uttam Kumar Ghorai[1]*

[1]Department of Industrial Chemistry & Applied Chemistry, Swami Vivekananda Research Centre, Ramakrishna Mission Vidyamandira, Belur Math, Howrah, 711202, India.

* E-mail: uttam.indchem@vidyamandira.ac.in

[2]Department of Physics, SRM University – AP, Amaravati, Andhra Pradesh, 522240, India.

Abstract: Using low and optimized magnetic field along with electric field is a novel strategy to facilitate electrochemical nitrite reduction. Here, we report for the first time on the synthesis of ammonia via magneto-electrocatalytic methods that use spin-thrusted β-MnPc in a magnetic field of 95 mT. The calculated rate of ammonia generation was 16603.4 µg h^{-1} mg$_{cat}$$^{-1}$, which is almost twice that of the non-polarized MnPc catalyst. Additionally, the faradaic efficiency at –0.9V vs. RHE was found to be 92.9%, significantly higher compared to the non-polarized MnPc catalyst. In presence of external magnetic field, MnPc catalysts provide a better electron transfer channel which results in a lower charge transfer resistance and hence better electrochemical performances. DFT result further verifies that magnetic field induced β-MnPc has a lower potential barrier (0.51 eV) for the protonation of NO* (PDS) than non-polarized β-MnPc (1.08 eV), which confirms the enhanced electrochemical nitrite reduction to ammonia aided by external magnetic field.

Keywords: Ammonia • nitrate reduction • electrochemistry • magnetic field • spin polarization

Introduction

Ammonia (NH_3) serves as a highly essential prized chemical ingredient in various agricultural and industrial applications, including fertilizers, textiles, and pretended fibers.[1,2,3] However, the current industrial production of ammonia predominantly relies on the energy-intensive Haber-Bosch process, which is accompanied by significant greenhouse gas emissions.[4,5] In recent years, electrocatalytic ammonia synthesis has emerged as a promising alternative to the Haber-Bosch process.[6] Furthermore, the increasing industrial development has resulted in more frequent emissions of NO_x, particularly nitrate (NO_3^-) and nitrite (NO_2^-), which contribute to environmental pollution.[7,8,9] Exploring the use of non-precious metals as catalysts for the reduction of nitrite (NO_2^-) to ammonia (NH_3) has gained more attention in recent years.[10,8,11,12] While noble metal-based materials like Ag[13], Pd[14,15], Ru[16,17], Mo[18], Ir[19], Au[20], and Pt[21] have demonstrated activity for NO2RR, their scarcity makes them costly for industrial applications. Instead of using ordinary experimental methods, using a common permanent magnet can have a substantial impact on a variety of chemical processes.[22] At a very low magnetic field intensity of 55 mT (600 times the Earth's magnetic field), for example, catalyst-based adenosine 5-triphosphate (ATP) synthesis rose by 50%.[23] Changes in reaction rates, which cause transitions between the triplet and singlet states of the reactant, are thought to be the cause of this magnetic field effect.[24] Additionally, when using ferromagnetic electrodes like Ni, Co, etc, the introduction of a modest magnetic field has demonstrated substantial improvements in the water-splitting kinetics.[25,26] Magnetohydrodynamics effects caused by the Lorentz force, which affect ionic currents and the formation and release of oxygen and hydrogen bubbles, can be used to explain the increase in catalytic efficiency independently of magnetism.[27,28] Consequently, magnetic field-assisted electro reactions have emerged as a state-of-the-art technique for electrochemical reactions linked to energy conversion, such as the OER[26,29], HER[30–32], ORR[33], CO2RR.[34,35] On the other hand, there hasn't been any research on using an external magnetic field to boost electrochemical ammonia synthesis as of yet. Mn, a transition metal, has exhibited exceptional catalytic activity in the oxidation and reduction of nitrogen because it has unpaired electrons in the d-orbital.[36] By leveraging the unpaired electron in the d-orbital in transition metal Mn and taking advantage of the paramagnetic intermediates of nitrite ions, electrocatalytic ammonia production during NO2RR can be significantly enhanced. Reactant electronic structures and energy levels are modified as a result of this alignment, changing the pace at which reactions occur. These elements support the reaction's catalytic activity and efficiency, which makes it a viable route for the production of ammonia in a sustainable manner.

Using manganese phthalocyanine, or MnPc, as a high-performance electrocatalyst for the reduction of NO_2-to-ammonia production is advised in light of this knowledge. Our investigation's primary focus is the employment of MnPc in 0.2 M Na_2SO_4 and 0.1 M NO_2^- solutions following a specific optimized magnetic field. MnPc exhibits a noteworthy NH_3 production of 16603.4 µg h^{-1} mg$_{cat.}^{-1}$ at –0.9V vs RHE

in the presence of a 95 mT external magnetic field, together with an unexpectedly high Faradaic efficiency (FE) of 92.9% of the sample. The efficiency of the Mn Centre of MnPc catalyst (host surface) as a potential determination step (PDS) is demonstrated by the reduction of NO_2^-, which occurs there with a low energy barrier of 0.51 eV, according to density functional theory (DFT) calculations.

Results and Discussion

Magnetic field interaction on β-MnPc

The aromatic macrocycle molecule manganese phthalocyanine (MnPc) has a core metal ion (Mn) that extends within and connects to the organic framework through four nitrogen centers. The d-orbitals of Mn in MnPc (**Scheme 1a**) change to: $a_{1g}(d_{z2})$, $b_{1g}(d_{x2-y2})$, $e_g(d_{zx}, d_{yz})$, and $b_{2g}(d_{xy})$.[37] In contrast, below a certain temperature (T_c), β-MnPc forms exhibit long-range ferromagnetism driven by feeble interactions between the chains.[37] Barraclough et al.[38] observed that intrachain ferromagnetic interactions predominate inside β-MnPc, with a value of $J/kB = 11K$ for Mn (II) S = 3/2. In **Fig. 1a**, β-MnPc showed ferromagnetism below $T_c \sim 8.6$ K, as demonstrated by the magnetization curves obtained with a superconducting quantum interference device (SQUID).[39] The M vs. H diagram for MnPc also shows that the saturation magnetization at 4K is ~9.6 emu/g (SI). Through magnetic exchange (**Scheme 1b-1c**), which creates low electronic repulsion and imparts a specific spin orientation to the adsorbed N species, spin polarization promotes the primary electron transfer step.[40,41] Numerous studies exist describing the tuning of intermediate radical pairs by an external magnetic field.[42,43] These radicals can exist in two different forms: singlet or triplet. Singlet and triplet radical pairs are in dynamic equilibrium [S↔T] with one another in the absence of an external magnetic field, preserving a constant statistical ratio.[44] The external magnetic field tuned this equilibrium from triplet to singlet.[42,43,44] The generation of the excess reactive singlet radical pair increases the catalytic yield. A greater likelihood exists that the increase of the NO_2RR process in the presence of an external magnetic field is due to this spin modulation of the intermediate radical pair. Along with this effect, the magnetohydrodynamic effect (MHD) may also play a dominant role in the enhancement of the ammonia yield. Magnetic field-assisted bubble removal frees up catalytic active sites and also hastens the catalytic process. All these effects, either separately or together, work to further boost NO_2RR activity. Due to this additional support by the magnetic field, the current density rises from NO_2^- to NH_3 at the same potential, which is known as the magneto-current effect (MCE).[45]

Synthesis and Characterization of β-MnPc

MnPc was synthesized by solvothermal technique; details are given in supporting information. X-Ray diffraction XRD curves (**Fig. 1b**) reveal that MnPc exhibits prominent diffraction peaks on the (100) and ($\bar{1}$02) planes, fully consistent with literature values (matched with ICDD card no #02–063–

3

3894).[39,46] High-angle annular dark-field scanning transmission electron microscopy (HAADF-STEM) shows the presence of Mn, C, and N elements in the MnPc system (**Fig. 1c**). FTIR (SI) and UV-vis spectroscopy (SI) measurements further confirmed several chemical bonds and distinct bands present in MnPc. Preliminary XPS survey scans (SI) clearly revealed the elemental composition of the catalyst, which consists of manganese (Mn), nitrogen (N), and carbon (C). A deeper dive into the high-resolution C 1s XPS spectrum (SI) revealed a prominent peak at 284.2 eV, indicating the presence of C1s in MnPc. The Mn–N bond of the pyridinic-N species at 398.4 eV and the pyrrolic-N species at 399.5 eV are the N species observed in the high-resolution N 1s XPS spectrum (**Fig. 1d**). In the high-resolution Mn 2p XPS spectrum (**Fig. 1e**), the Mn $2p_{3/2}$ species appeared as a peak at 641.8 eV, while the Mn $2p_{1/2}$ species was detected at 653.4 eV.[46]
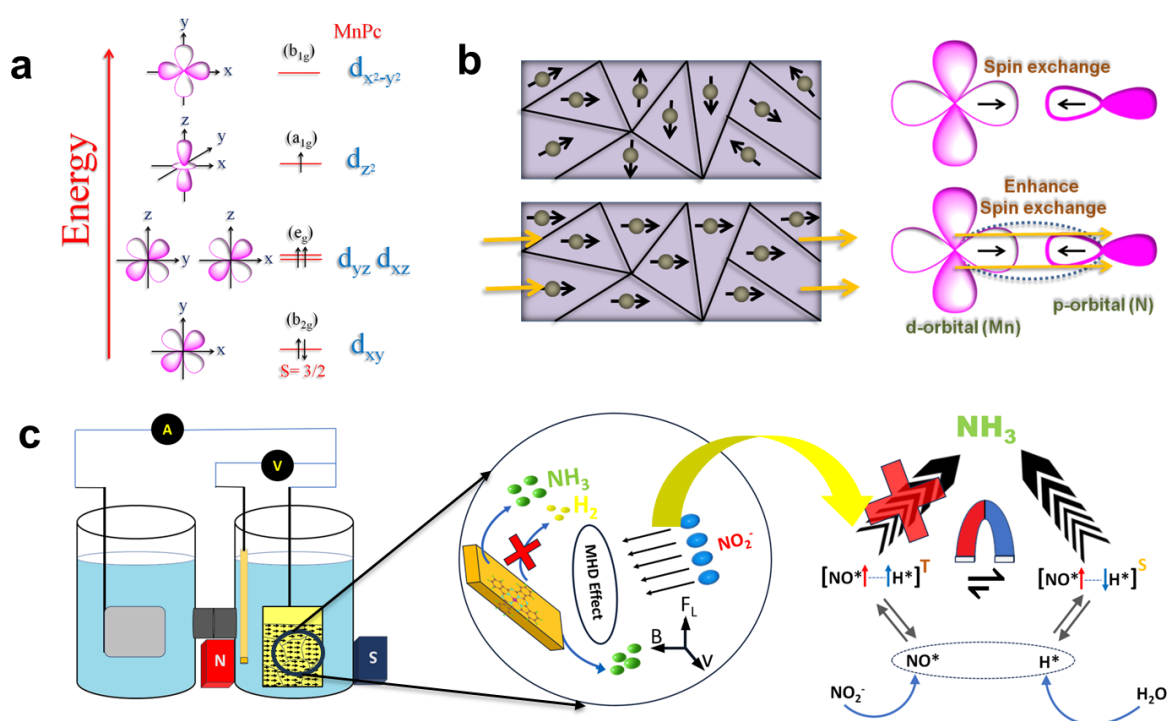
Scheme 1 | Schematic representation of effect of magnetic field on MnPc. a. MO of MnPc. **b.** Plausible spin exchange process during applied magnetic field. **c.** Spin magnetic effect under a magnetic field in MnPc electrocatalyst

Using synchrotron X-ray absorption spectroscopy (XAS), the catalyst's atomic-level structure was fully investigated, with a particular emphasis on the Mn K-edge X-ray absorption near-edge structure (XANES). The Mn-phthalocyanine (MnPc) catalyst displayed distinct spectral features akin to those observed in the reference samples of pure Mn foil and MnO_2.

https://doi.org/10.26434/chemrxiv-2024-v8chs **ORCID:** https://orcid.org/0000-0003-0537-598X Content not peer-reviewed by ChemRxiv. **License:** CC BY-NC-ND 4.0
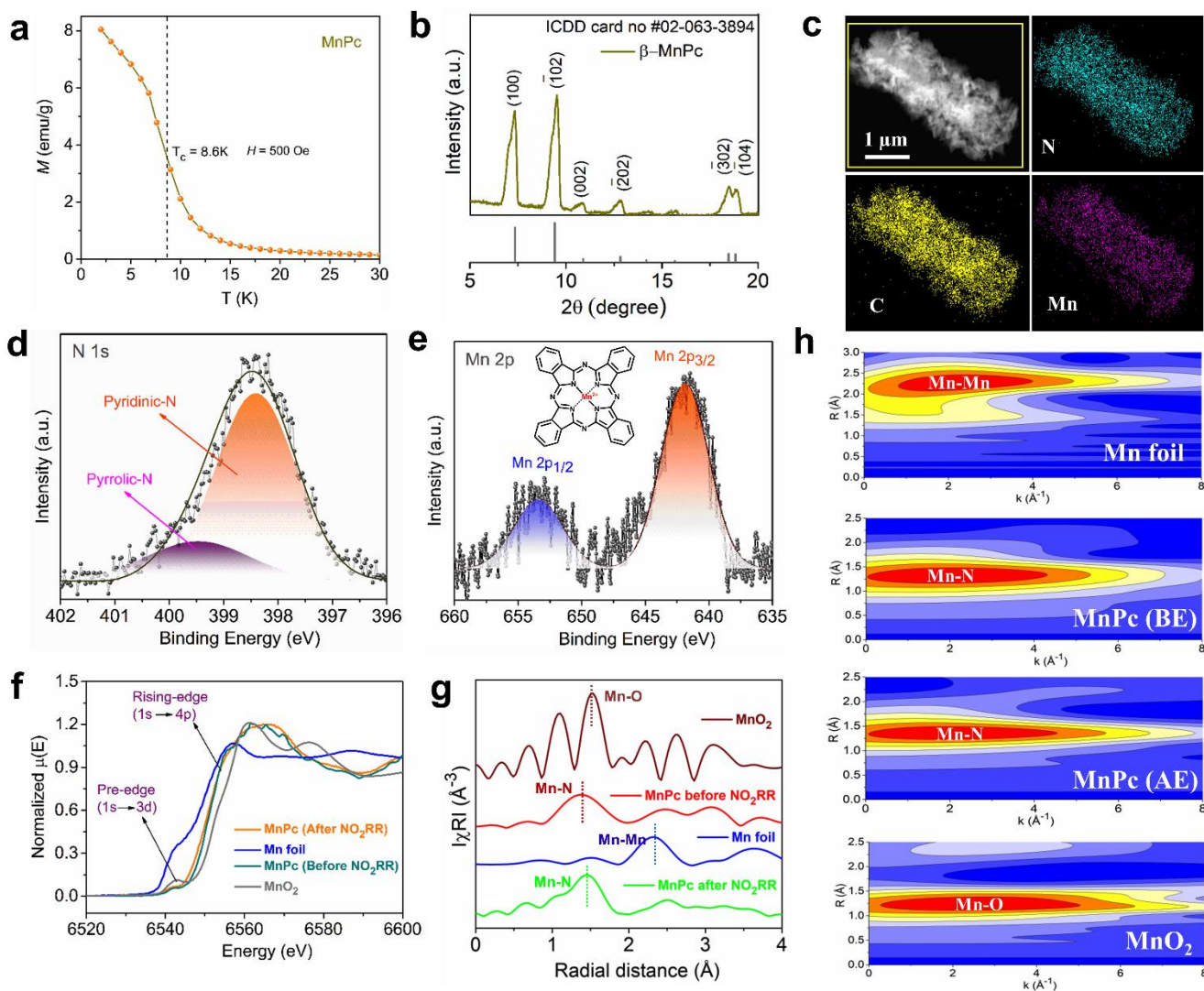
Fig. 1 | Structural characterization of MnPc. a. M-T plot of MnPc. **b.** XRD plot of MnPc. **c.** HAADF-STEM of MnPc. **d.** High resolution XPS N1s spectra of MnPc. **e.** High resolution XPS Mn 2p spectra of MnPc. **f.** XANES spectra at Mn *K*-edge. **g.** EXAFS spectra at Mn *K*-edge. **h.** WT of Mn foil, MnPc (before electrolysis), MnPc (after electrolysis), and MnO_2 (from up to down).

From synchrotron X-ray absorption spectroscopy (XAS) (**Fig. 1f**), the MnPc (both before and after electrolysis) absorption edge position fell between that of Mn foil and MnO_2, indicating that the valence state of manganese in MnPc is less than +4.[47,48] A Mn pre-edge absorption peak in XANES is observed at ~6541.5 eV due to the 1s to 3d electronic transition and the rising Mn edge peak is due to the 1s to 4p transition at ~6562 eV in MnPc system. The Fourier transformed (FT) extended X-ray absorption fine structure (EXAFS) analysis of MnPc (both before and after electrolysis) unveiled a prominent peak at ~1.49 Å (as depicted in **Fig. 1g**), according to the manganese and nitrogen atoms' symmetrical scattering interaction inside the MnPc molecule (SI). Surprisingly, the lack of a signal related to Mn-Mn scattering at about ~2.3 Å indicated that manganese was atomically distributed in MnPc. A peak at ~1.53 Å confirmed the presence of Mn-O bond scattering in MnO_2. The C scattering path in higher coordination shells with Mn was identified as the cause of another peak, which was found at roughly

~2.5 Å.[47,49] Moreover, the results of wavelet transforms (WT), which are shown in **Fig. 1h**, offered more proof that the MnPc catalyst has Mn-N bonding, which peaks at about 2 Å^{-1} and sets it apart from Mn foil.[47,48]

DFT Modulation of Electron Spin Exchange Interaction

Density functional theory (DFT) helps us comprehend the chemical reaction of NO$_2$RR on MnPc catalyst by computing the total energy of each and every possible intermediate, electronic structure, charge density difference etc. The Mn centre on MnPc is confirmed by DFT investigations to be more active towards NO$_2$RR than other potential centres (SI). The transition metal atom's valence d-orbitals give off charges to NO$_2$, which reduces when it approaches and settles on the active metal core. The quantitative approach of calculating the charges associated with the main active site (Mn), before and after adsorption of NO$_2$, are estimated to be 5.74e and 5.6e respectively. Accumulation and loss of charges by respective atoms, have been presented through charge density difference plot (see SI). Analyse of the partial density of states (PDOS)[46,50] plots, reveals that, following the adsorption of NO$_2$, the d-band centre shifts from 3.34 eV to 3.15 eV (see SI), pointing to the charge transfer that took place between Mn and the closest nitrogen (N) and the deposited NO$_2$ molecule. One side reaction (HER), which is a two-electron transfer process, might take into part and hamper the main reaction (NO$_2$RR) by getting adsorbed of H on the active sites. To suppress this parallel reaction, any of the two conditions[51] is to be satisfied for the main reaction to be occurred: (1) limiting potential of NO$_2$RR must be less than the HER and (2) $\Delta G*NO_2H$ should be more negative than $\Delta G*H$. Here, we have performed the calculation for two different conditions for the same system (MnPc), one is without spin polarized approach (named as condition A) and another one with spin polarized approach, taking into account the initial magnetic moment (named as condition B). We have performed (under condition B) Crystal Orbital Hamiltonian Population (COHP) calculation[52,53] (**Fig. 2b**) of nearest single Mn-N contact to examine NO$_2$ (**Fig. 2c**) adsorption over HER (**Fig. 2d**), where we found that the NO$_2$ adsorption, based on ICOHP (integrated crystal orbital Hamiltonian population) values[54] is stronger (ICOPH value decreases from -1.27 to -1.24) than hydrogen atom adsorption (ICOPH value increases from -1.27 to -1.29) (see **Fig. 2a-2e**). The experimental (gas chromatography) finding further demonstrates that, in comparison to NO$_2$RR, the HER is reduced when a magnetic field is provided at a specific distance from the working electrode in MnPc (SI), which is similar to the prediction made by the theoretical DFT calculation.
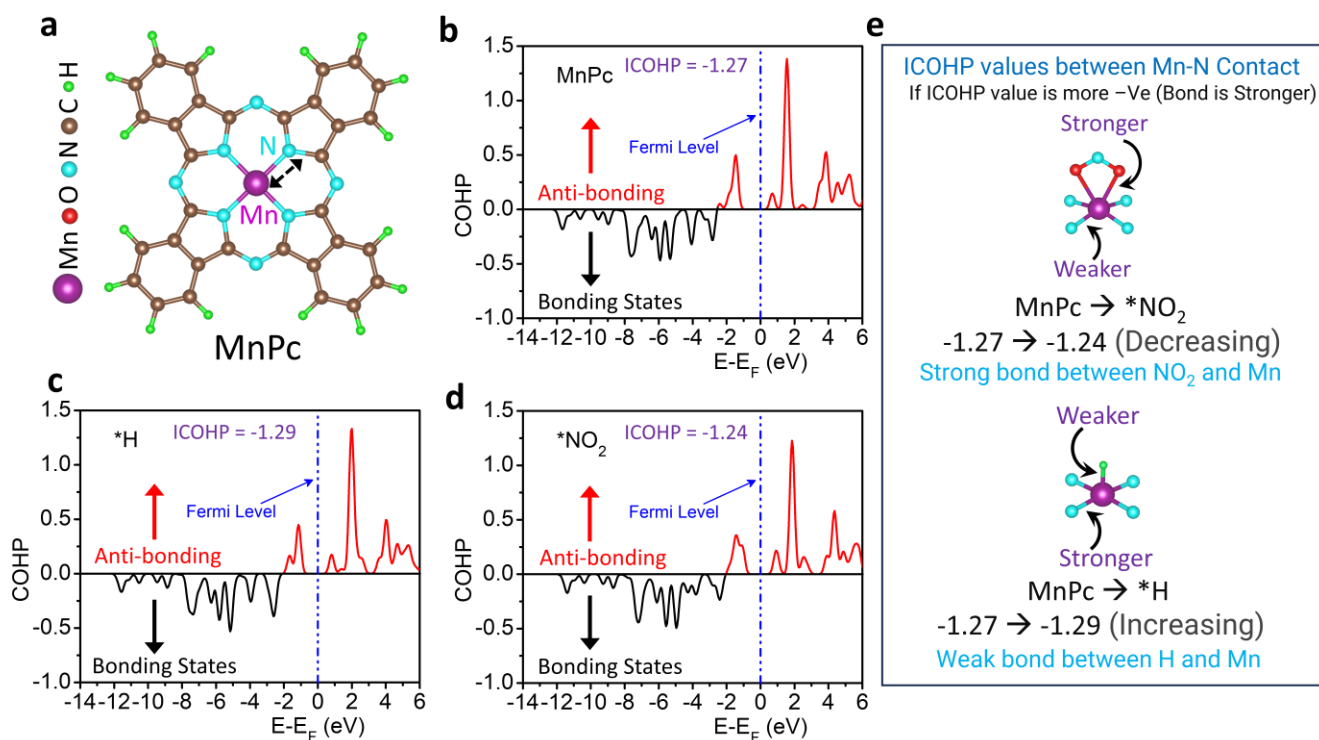
Fig. 2 | DFT modulation study of *H and *NO$_2$ adsorbed on Mn of MnPc. a. Mn-N contact shown for the optimised structure of MnPc catalyst. **b.** COHP calculations to check the bond strength of Mn-N contact for without any atom or molecule adsorbed on the active site. **c.** COHP for H adsorbed on Mn of MnPc. **d.** COHP for NO$_2$ adsorbed on Mn of MnPc. **e.** demonstration of COHP calculations with ICOHP values. (Considering the system with spin polarized plus intrinsic magnetic moment).

To further evaluate the hydrogenation ability with NO$_2^-$ with and without a magnetic field, we performed an EPR experiment. The H·trapping agent 2,2,6,6-tetramethyl-1-piperidinyloxy (TEMPO) was used for better understanding. MnPc in the presence of a magnetic field (with 0.2 M SO$_4^-$ and in a NO$_2$-free electrolyte), shows a stronger TEMPO-H signal than MnPc without any magnetic field (SI), suggesting that MnPc (with 95 mT) is more effective than MnPc (with 0 mT) in dissociating H$_2$O and generating H radicals.[55–57] Nevertheless, the TEMPO-H signal intensity of MnPc (with 0 mT) decreased when 0.1 M NO$_2^-$ was added to the system, whereas the TEMPO-H signal of MnPc (with 95 mT) highest decreased (SI), suggesting MnPc (with 95 mT) increases the hydrogenation in NO$_2^-$ by consumes H radicals to form ammonia.

From the perspective of adsorption free energy, we observed that in conditions A and B, the NO$_2$ molecule is more advantageous than the hydrogen atom on the Mn centre of the MnPc catalyst, indicating that the reaction selectivity shifts in the direction of NO$_2$RR as shown in **Fig. 3a**. We can see the values of adsorption free energy changes of NO$_2$ in the two conditions are -2.12 eV (for A) and -1.18 eV (for B). To explain the protonation of NO$_2$RR, for both the cases (without and with spin polarized), we have investigated H-adsorption on five probable potential sites including Mn-centre (see **Fig. 3b**) which may help in the hydrogenation for the same. In case of "without spin", we have 1.08V as

the limiting potential for NO_2RR where Mn-centre is chosen as promising active site for the reaction mechanism. As NO_2 is already adsorbed, because of higher binding energy (see **Fig. 2**) than H-atom, the chance of H-adsorption on the Mn-centre is less or blocked by pre-adsorbed NO_2. Therefore, other four sites: pyrrolic N1, pyrrolic N2, Pyridinic N and nearest C to Mn-centre may help in the protonation having adsorption free free energies -0.53, -0.53, -0.51 and 0.11eV respectively. Out of four sites C site near to Mn-centre, having positive H-adsorption free energy (0.11eV), also will be good enough to adsorb H and help in the protonation for NO_2RR mechanism, because NO_2RR requires 1.08eV as activation energy to be happened. On the other hand, for spin polarized case (see **Fig. 3c**), we have 0.51V as the limiting potential for NO_2RR and Mn-centre is the main active site. Herein, also NO_2 is bound on Mn-centre and blocked the H-atom like "without spin" case. For other four probable sites: pyrrolic N1, pyrrolic N2, Pyridinic N and nearest C to Mn-centre having free energies 1.18, 1.18, -0.12 and 0.46eV respectively, we observed that out of four sites pyrrolic N1 and N2 having more positive free energy even greater than the limiting potential of NO_2RR, indicating these two sites will be unable to adsorb H-atom even at the applied activation potential of 0.51V. So, in case of spin polarized system, pyridinic Nitrogen and C-site near to Mn-centre may help in the protonation for NO_2RR as having less H-adsorption free energy than the limitng potential of NO_2RR mechanism.

In order to understand the thermodynamics of the non-electrochemical reaction mechanism of NO_2RR on the provided catalyst, we have selected three known potential pathways (SI), which have been reported in the literature[51] for metal surfaces, single atom catalysts, etc., where the protonation step has been identified as the second step of the potential reaction pathway, i.e., $NO_2 \rightarrow *NO_2 \rightarrow NO_2H$. Stability of all the intermediate states are checked with DFT and corresponding free energy values are improved through correction term (E_{ZPE-TS}) (given in the SI). Through Path I, the most advantageous method determined by the lowest ΔG of potential determining step among all conceivable pathways for NO_2RR, we have shown the whole free energy profile along with optimised intermediates **(Fig. 3e)**.

In the free energy diagram, we can see step 1 $\rightarrow$ step 2 is exothermic in nature for both conditions (A and B) which tells us NO_2 approaches onto the metal site and gets adsorbed without facing any difficulties, forming the intermediate *NO. Next to it, protonation starts taking place and reaches to the step 4 by releasing a water molecule ($*NO_2H + 2H^+ + 2e^- \rightarrow *NO + H_2O$) possessing a -0.02 eV shift in free energy (step 2 for A), -0.51 eV (step 2 for B) and 1.74 eV (step 3 for A), -2.31 eV (step 3 for B), respectively. At step $NO* \rightarrow *NOH$ creates positive variation of thermodynamic free energy (endothermic process) which is measured to be the highest uphill in the free energy profile, known as limiting potential or potential determining step (PDS) of the NO_2RR, with free energy change of 1.08 eV and 0.51 eV for the conditions A and B respectively. The results indicate that the intrinsic magnetic moment helps lowering (from 1.08 eV to 0.51 eV) the electrochemical limiting potential barrier of NO_2RR. In the next, a series of intermediates follow downhill trend up to step 9 caused by serially

8

interaction with ($H^+ + e^-$) pair, for both conditions (A and B). At last, for spin polarized plus magnetism-based approach (condition B), NH_3 released through desorption process (exothermic), from the surface of catalyst, in much faster way than the without spin polarized based approach (condition A) having an endothermic barrier.
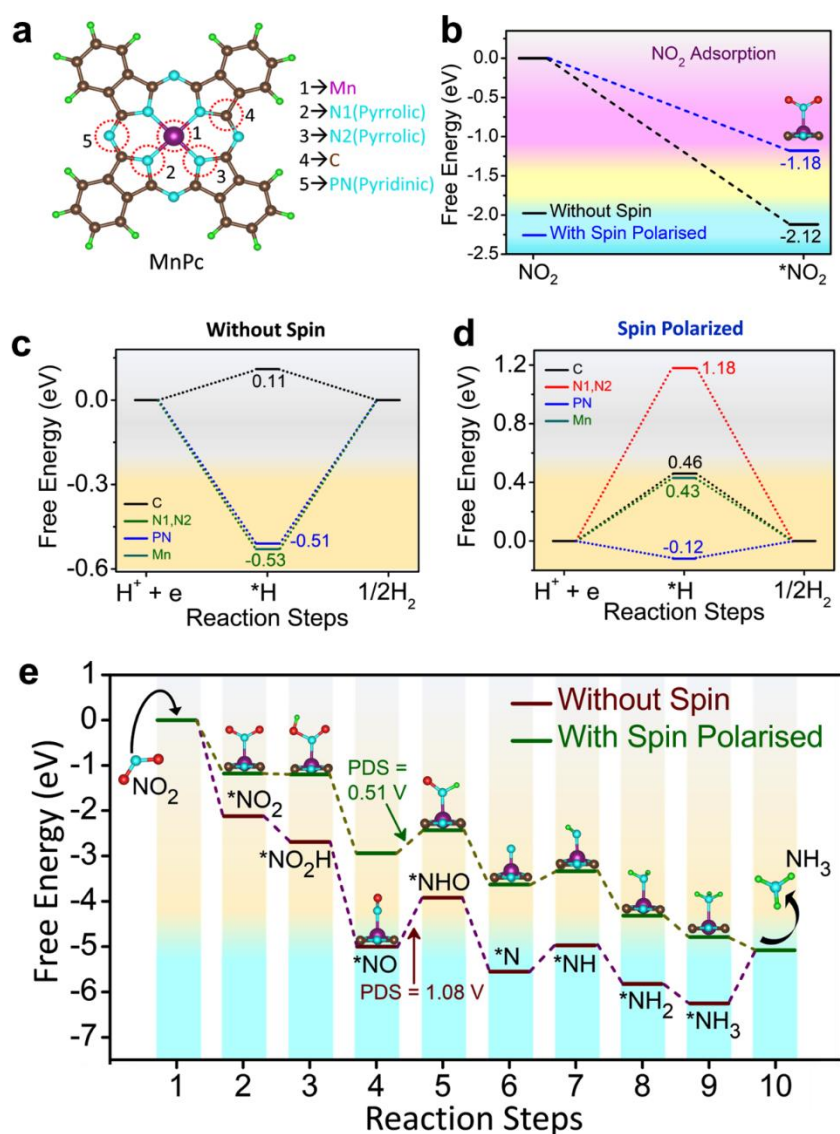

Fig. 3 | DFT modulation study on ammonia formation. a. Represents the optimized structure of MnPc having red marked circles for NO_2 and H-adsorption as probable active sites, **b.** represents the comparison of NO_2 adsorption free energies under condition A and condition B respectively, **c.** and **d.** show the comparison of H-adsorption on MnPc for the mentioned two conditions, **e.** displays the full free energy profile along with most favourable pathway under condition A and condition B.

Electrocatalytic performance for ammonia synthesis

With an electrolyte of 0.1 M $NaNO_2$ and 0.2 M Na_2SO_4, all electrochemical experiments were tested in a basic H-type cell using a traditional three-electrode electrochemical setup. MnPc was coated on carbon paper, Pt foil, and Ag/AgCl for the working electrode, counter electrode, and reference electrode, respectively. The ammonia yield rate and Faradaic efficiency were determined by running the

9

experiments for thirty minutes. Chronoamperometry measurements were conducted across a range of electrode potentials, as shown in SI. In the presence of $NaNO_2$, the current density (linear sweep voltammetry, **Fig. 4a**) was increased in tandem with external magnetic field. Electrochemical impedance spectroscopy (EIS) data were used to further investigate the reasons for the exceptional performance of MnPc for selective nitrite reduction to ammonia. The equivalent circuit, which consists of a solution resistance (R_s) connected to the R–C circuit (R_{ct} and C_{dl}), was used to match the Nyquist plots (**Fig. 4b**). It shows that with increasing magnetic field up to 95 mT, the semicircle corresponding to the charge transfer (CT) resistance (R_{ct}) of the electrolytic medium decreases (**Fig. 4c,** SI), which facilitates the nitrite conversion reaction on the catalyst surface. This result is further supported by the c_{dl} value calculated from the cyclic voltametric diagram (SI). The levels of ammonia (NH_3) and hydrazine (N_2H_4, potentially by-products) in the electrolyte solution were measured using the indophenol blue technique and the Watt and Chrisp method, respectively (SI). Notably, both the NH_3 yield and the Faradaic efficiency (FE) increase with increasing cathodic potential, eventually reaching their maximum values of 8266.5 $\mu g h^{-1} mg_{cat}^{-1}$ and 74.55% at –0.9 V vs RHE, respectively (**Fig. 4d**). The results were increased almost 2-fold when 95 mT magnetic field was applied at –0.9 V vs. RHE reaching an ammonia yield rate of 16603.4 $\mu g h^{-1} mg_{cat}^{-1}$ and FE of 92.9%, respectively (**Fig. 4e**) (SI). Ion chromatography was used to further confirm the ammonia result, and the results indicated no discernible difference between the two (SI). The results obtained are comparable to the literature (SI). We have also observed that after removing the external magnetic field after some magnetic incubation time (SI), the MnPc catalyst shows slightly better catalytic performance than the non-magnetized MnPc catalyst. We also examined the turnover frequency (TOF) (**Fig. 4f,** SI) and long-term stability (SI) of MnPc for real-life application of the catalyst. The findings demonstrate that when an external magnetic field of 95 mT was applied to MnPc, the TOF value increased from ~0.15 s^{-1} to ~0.3 s^{-1} (SI). Also, the MnPc catalyst showed 50-h stability without much fluctuation of the current density during NO_2RR @– 0.9V with 95 mT. After the NO_2RR test, we tested the catalyst stability using XPS analysis and the results show that the results are almost identical to the pre-NO_2RR test (SI).
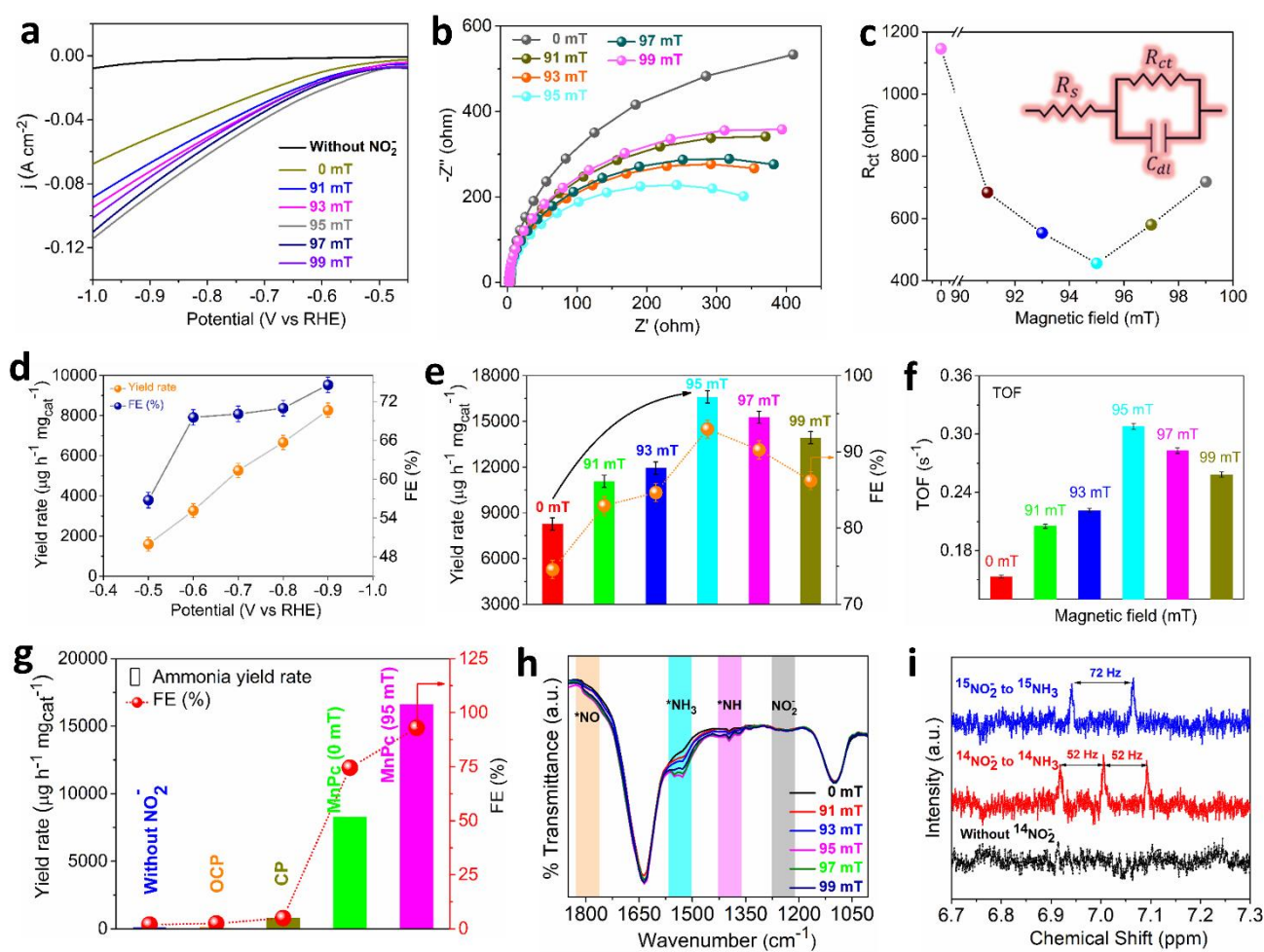
Fig. 4 | Electrochemical performance. a. LSV plot of MnPc with varying magnetic field. **b.** EIS spectra after simulation of MnPc with varying magnetic field. **c.** R_{ct} vs. Magnetic field diagram of MnPc. **d.** Ammonia yield rate and FE at various potential without applying magnetic field. **e.** Ammonia yield rate and FE with applying magnetic field @–0.9 V vs. RHE. **f.** TOF (s^{-1}) plot of MnPc for NO_2RR at various applied magnetic fields @–0.9V. **g.** Various control experiment of MnPc @–0.9V vs RHE. **h.** ATR-FTIR spectroscopy of electrolytes solution @–0.9V vs RHE. **i.** Isotopic labelling experiment of the electrolyte's solution after electrolysis @–0.9V vs RHE (50-time dilution).

Additionally, control experiments (**Fig. 4g**) confirmed that ammonia is not formed in the electrolyte without nitrite ions @–0.9V vs RHE or during OCP experiments when nitrite ions are present @95 mT magnetic field. However, when nitrite ions were present in the electrolyte, we observed certain ammonia production. Additionally, ATR-FTIR spectroscopy confirmed that a notable vibrational bond signal was present at 1528 cm^{-1}, indicating the existence of *NH$_3$. Main intermediate products are assigned as *NO at 1790 cm^{-1} and *NH at 1396 cm^{-1} (**Fig. 4h**).[46,58] A vibrational band was detected at 1635 cm^{-1} as a result of H$_2$O's O-H bending. The presence of nitrite in the medium is supported by an FTIR vibrational band at 1237 cm^{-1}.[59] In the ^{1}H–NMR spectrum, when we use $^{15}NO_2^-$, we observe the characteristic double peak of $^{15}NH_4^+$. On the other hand, when $^{14}NO_2^-$ was used, the ^{1}H–NMR spectra

exhibited triple peaks of $^{14}NH_4^+$ (**Fig. 4i**) and no such peak was observed in the NO_2^- free electrolyte @-0.9V vs RHE.

Methods

Synthesis of MnPc

MnPc were synthesized using a solvothermal technique. For this method, the precursor solution was made up of 8.64 mmol of phthalonitrile, 30 mg of ammonium heptamolybdate tetrahydrate, 2.16 mmol of manganese acetate, and 72 mL of solvent made of ethylene glycol. To guarantee complete mixing prior to nucleation, the liquid mixture was agitated for ten to fifteen minutes at 60 °C. Subsequently, the solution was moved into a 100 mL Teflon autoclave cup and heated to 180 °C for a full day (24 Hours) of solvothermal treatment. Whatman 41 filter paper was used to filter the solution after it cooled in order to get rid of any leftovers. After that, all contaminants were completely removed from the residual precipitate by extensively washing it in hot water, ethanol, and 0.1 M HCl. In order to get a dry powder that was ready for use again, the acquired MnPc sample was finally dried for 12 hours at 65 °C.

Characterization technique

X-ray diffraction (XRD) was used to analyse the synthesised MnPc's crystal structure and phase purity. XRD analysis was performed using a Bruker D-8 X-ray powder diffractometer equipped with an advanced Eco X-ray system. Cu-K_α monochromatic radiation with a wavelength of 0.15404 nm was used. The voltage and current used to run the X-ray tube were 40 kV and 25 mA, respectively. To investigate the electronic structure and chemical composition of MnPc, X-ray photoelectron spectroscopy (XPS) analysis was conducted using an OMICRON-0571 framework. This technique provides valuable information about the oxidation states and bonding environments of the elements in the material. Through the use of Fourier-transform infrared (FTIR) research, the different kinds of chemical bonds found in MnPc were determined. This analysis was carried out using a Shimadzu IRAffinity-1S instrument, which allows for the characterization of molecular vibrations and the determination of functional groups. The morphology of the synthesized MnPc was observed using a Thermo Scientific Apreo-S field emission scanning electron microscope (FE-SEM). This instrument enables high-resolution imaging of the sample surface, providing insights into the size, shape, and surface morphology of the MnPc nanostructures. For electrochemical nitrogen oxidation analyses, the CHI 760E equipment was utilized. The Metrohm Echo IC (ion chromatography) instrument and Agilent 8860 GC system were used for the detection of ammonium ions and H_2 gas. A neodymium block magnet (NdFeB) was used as a permanent magnet for the magneto-reduction process. The magnetic field was measured using a Digital Gauss Meter instrument (DGM-102). A Quantum Design MPMS3 superconducting quantum interference device (SQUID) magnetometer was used to measure the MT and

https://doi.org/10.26434/chemrxiv-2024-v8chs **ORCID:** https://orcid.org/0000-0003-0537-598X Content not peer-reviewed by ChemRxiv. **License:** CC BY-NC-ND 4.0

MH diagrams of MnPc. This instrument allowed for the measurement and analysis of the electrochemical behavior of MnPc, particularly its performance in nitrite reduction reaction.

Experimental Setup

The electrochemical measurements for the nitrite reduction reaction (NO$_2$RR) were performed using the CHI 760E electrochemical workstation. An H-type cell configuration was employed, with a Nafion 117 membrane serving as the separator between the anode and cathode compartments. The components of the reference electrode, counter electrode, and working electrode were Ag/AgCl, a platinum foil, and MnPc (1 x 0.8 cm^2 in carbon paper) respectively. The electrolyte solution utilized in the experiments consisted of Na$_2$SO$_4$ with and without NO$_2^-$ solutions. This allowed for the investigation of the NO$_2$RR under different conditions and concentrations. To ensure accurate comparisons, the geometric area of the electrode surface was utilized to normalize the current density.

Catalyst ink/working electrode preparation

2 mg of synthesized MnPc and 100 μL of Merck-sourced 2-propanol were mixed to prepare the catalytic ink for magneto-electrochemical nitrite reduction, which was then sonicated for one minute. Next, to ensure even mixing, 10 µL of Sigma Aldrich's 5 weight percent Nafion 117 solution was added to the mixture and vortexed for five minutes. Next, 25 μL of the applied ink was placed on a 1 x 0.8 cm^2 carbon paper substrate for NO$_2$RR application.

Formulas for calculation

The NH$_3$ yield rate was calculated using the following equation:

$$\text{NH}_3 \text{ yield rate} = \frac{(C_{NH_3} \times V)}{(m_{NH_3} \times t)}$$

Here, C_{NH_3} represents the concentration of NH$_3$, V is the volume of the reaction electrolyte, m_{NH_3} denotes the catalyst mass loaded on working electrode, t represents the electrolysis time.

The Faradaic efficiency (FE) was determined using the following equation:

$$\text{FE}(\%) = \frac{(6 \times F \times C_{NH_3} \times V)}{(M_{NH_3} \times Q)} \times 100\%$$

Here, F corresponds to the Faraday constant (96,485 C mol^{-1}), M_{NH_3} denotes the molar mass of ammonia, and Q signifies the total charge.

Computational Details

Density functional theory based VASP computational code is used for the required findings in our theoretical studies. A maximum kinetic energy cut-off of 450 eV is selected for the plane wave[60] expansions that are under consideration. Convergence criteria for ionic and electronic optimisations are fitted to be $1E^{-5}$ eV, meaning that the computation converges when the energy difference between two successive electronic or ionic steps is $1E^{-5}$ eV, in order to obtain the ground state energy of all feasible intermediates. For the finding of ZPE of free molecules and adsorbed molecules it is $1E^{-08}$ eV. Ionic convergence criteria for stability checking of each intermediate are -0.001 eV/Å and the same for ZPE, we have used as -0.00001 eV/Å. The General Gradient Approximation of PBE functional is used to treat the existence of exchange and correlation forces among electrons in the given system. [61] The Projected Augmented Wave technique is used to demonstrate the interactions between the freezing core and the valence electrons. By introducing the Grimme DFT-D2 dispersion scheme, we have also taken into account the effects of long-range weak Van der Waal forces among atoms in the system in order to obtain accurate energy estimates.[62] We have used Gamma centre K-point sampling for the zero-dimensional system in order to optimise and perform PDOS computations.

Conclusion

In conclusion, theoretical calculations as well as experimental results confirm that exoteric magnetic field-induced spin-polarised MnPc has tremendous NO_2RR activity. MnPc, in presence of 95 mT external magnetic field shows a significantly higher ammonia yield rate of 16603.4 µg h^{-1} mg$_{cat}$$^{-1}$ and Faradaic efficiency of 92.9% at –0.9V vs. RHE, which is almost twice that of the MnPc catalyst. A spin-polarized Mn-N centre was argued to be able to specify spin electrons to interact with the reaction intermediates and, as a result, strengthen adsorption to produce the desired ammonia, so enabling the hydrogenation of *NO. Besides, we can infer that the diligence of magnetic spin-polarisation system facilitate the electron transfer, which results in enhancement of the reaction kinetics not only for NO_2RR but also for various other electrochemical reactions.

Acknowledgements

Technology for providing computational supports. The authors wish to thank the IACS-Kolkata & RRCAT-Indore for providing the instrumental facilities.

Author Contributions

UKG conceived the idea and designed the experiments. AA synthesized the catalyst and performed the XRD, FTIR, UV-vis. AA and KM carried out all the electrochemical measurements and analyzed the results. NB and RT performed the theoretical (DFT) calculations. RT, NB, UKG and AA analyzed the DFT results. AA and SB analyzed the NMR result. AA and SB analyzed the XANES and EXAFS. AA and KM analyzed the XPS results. All authors contributed to write the final version of the manuscript. UKG supervised the project.

Competing interests

UKG, AA and KM have filed an Indian Patent application (202431017396) regarding the magneto-electrochemical synthesis of ammonia under ambient conditions. The remaining authors declare no competing interests.

References

1. Dai, J. *et al.* Spin polarized Fe1−Ti pairs for highly efficient electroreduction nitrate to ammonia. *Nat. Commun. 2024 151* **15**, 1–11 (2024).

2. Chen, J. G. *et al.* Beyond fossil fuel-driven nitrogen transformations. *Science* **360**, (2018).

3. Fang, J. Y. *et al.* Ampere-level current density ammonia electrochemical synthesis using CuCo nanosheets simulating nitrite reductase bifunctional nature. *Nat. Commun.* **13**, 1–13 (2022).

4. Tang, C. & Qiao, S. Z. How to explore ambient electrocatalytic nitrogen reduction reliably and insightfully. *Chem. Soc. Rev.* **48**, 3166–3180 (2019).

5. Zheng, J. *et al.* Tuning the Electron Localization of Gold Enables the Control of Nitrogen-to-Ammonia Fixation. *Angew. Chemie Int. Ed.* **58**, 18604–18609 (2019).

6. Ghorai, U. K. *et al.* Scalable Production of Cobalt Phthalocyanine Nanotubes: Efficient and Robust Hollow Electrocatalyst for Ammonia Synthesis at Room Temperature. *ACS Nano* **15**, 5230–5239 (2021).

7. Zakem, E. J. *et al.* Ecological control of nitrite in the upper ocean. *Nat. Commun. 2018 91* **9**, 1–13 (2018).

8. Wan, Y., Zhang, Y., Zhang, N., Zhang, Z. & Chu, K. Single-atom Zn on MnO2 for selective nitrite electrolysis to ammonia. *Chem. Eng. J.* **481**, 148734 (2024).

9. John, J., MacFarlane, D. R. & Simonov, A. N. The why and how of NOx electroreduction to ammonia. *Nat. Catal.* **6**, 1125–1130 (2023).

10. Wang, H. *et al.* V-doped TiO2 nanobelt array for high-efficiency electrocatalytic nitrite reduction to ammonia. *Mater. Today Phys.* **30**, 100944 (2023).

11. Zhang, A. *et al.* High-Performance Electrocatalytic Reduction of Nitrite to Ammonia under Ambient Conditions on a FeP@TiO2 Nanoribbon Array. *Inorg. Chem.* **62**, 12644–12649 (2023).

12. Murphy, E. *et al.* Elucidating electrochemical nitrate and nitrite reduction over atomically-dispersed transition metal sites. *Nat. Commun.* **14**, 4–6 (2023).

13. Troutman, J. P. *et al.* PdAg Alloy Nanocatalysts: Toward Economically Viable Nitrite Reduction in Drinking Water. *ACS Catal.* **10**, 7979–7989 (2020).

14. Shin, H., Jung, S., Bae, S., Lee, W. & Kim, H. Nitrite reduction mechanism on a Pd surface. *Environ. Sci. Technol.* **48**, 12768–12774 (2014).

15. Chinthaginjala, J. K., Villa, A., Su, D. S., Mojet, B. L. & Lefferts, L. Nitrite reduction over Pd supported CNFs: Metal particle size effect on selectivity. *Catal. Today* **183**, 119–123 (2012).

16. Huo, X., Van Hoomissen, D. J., Liu, J., Vyas, S. & Strathmann, T. J. Hydrogenation of aqueous nitrate and nitrite with ruthenium catalysts. *Appl. Catal. B Environ.* **211**, 188–198 (2017).

17. Wang, F. *et al.* Electroreduction of Nitrite to Ammonia Over Ni1Ru Single-Atom Alloys. *Adv. Funct. Mater.* **34**, 2308072 (2024).

18. Wang, G. *et al.* Ambient ammonia production via electrocatalytic nitrite reduction over MoO2 nanoparticles self-supported on molybdenum plate. *Colloids Surfaces A Physicochem. Eng. Asp.* **657**, 130549 (2023).

19. Li, H. *et al.* Cu xIr1- xNanoalloy Catalysts Achieve near 100% Selectivity for Aqueous Nitrite Reduction to NH3. *ACS Catal.* **10**, 7915–7921 (2020).

20. Li, H., Guo, S., Shin, K., Wong, M. S. & Henkelman, G. Design of a Pd-Au Nitrite Reduction Catalyst by Identifying and Optimizing Active Ensembles. *ACS Catal.* **9**, 7957–7966 (2019).

21. Figueiredo, M. C., Climent, V. & Feliu, J. M. Nitrite Reduction on Bismuth Modified Pt(111) Surfaces in Different Electrolytic Media. *Electrocatalysis* **2**, 255–262 (2011).

22. Mitra, K., Adalder, A., Mandal, S. & Ghorai, U. K. Enhancing Electrochemical Reactivity with Magnetic Fields: Unraveling the Role of Magneto-Electrochemistry. *Small Methods* 2301132 (2024) doi:10.1002/smtd.202301132.

23. Buchachenko, A. L. & Kuznetsov, D. A. Magnetic field affects enzymatic ATP synthesis. *J. Am. Chem. Soc.* **130**, 12868–12869 (2008).

24. Steiner, U. E. & Ulrich, T. Magnetic Field Effects in Chemical Kinetics and Related Phenomena. *Chem. Rev.* **89**, 51–147 (1989).

25. Lin, M. Y., Hourng, L. W. & Kuo, C. W. The effect of magnetic force on hydrogen production efficiency in water electrolysis. *Int. J. Hydrogen Energy* **37**, 1311–1320 (2012).

26. Yan, J. *et al.* Direct Magnetic Reinforcement of Electrocatalytic ORR/OER with Electromagnetic

Induction of Magnetic Catalysts. *Adv. Mater.* **33**, 2007525 (2021).

27. Li, G. *et al.* Magnetocatalysis: The Interplay between the Magnetic Field and Electrocatalysis. *CCS Chem.* **3**, 2259–2267 (2021).

28. Wang, K. *et al.* Magnetic field induced motion behavior of gas bubbles in liquid. *Sci. Reports 2016 61* **6**, 1–6 (2016).

29. Wu, T. *et al.* Spin pinning effect to reconstructed oxyhydroxide layer on ferromagnetic oxides for enhanced water oxidation. *Nat. Commun. 2021 121* **12**, 1–11 (2021).

30. Saha, J., Ball, R. & Subramaniam, C. Premagnetized Carbon-Catalyst Interface Delivering 650% Enhancement in Electrocatalytic Kinetics of Hydrogen Evolution Reaction. *ACS Sustain. Chem. Eng.* **9**, 7792–7802 (2021).

31. Shetty, S. & Hegde, A. C. Magnetically Induced Electrodeposition of Ni-Mo Alloy for Hydrogen Evolution Reaction. *Electrocatalysis* **8**, 179–188 (2017).

32. Zhou, W. *et al.* Magnetic Enhancement for Hydrogen Evolution Reaction on Ferromagnetic MoS2 Catalyst. *Nano Lett.* **20**, 2923–2930 (2020).

33. Lu, F. *et al.* Regulation of oxygen reduction reaction by the magnetic effect of L10-PtFe alloy. *Appl. Catal. B Environ.* **278**, 119332 (2020).

34. Bhargava, S. S. *et al.* Decreasing the Energy Consumption of the CO2Electrolysis Process Using a Magnetic Field. *ACS Energy Lett.* **6**, 2427–2433 (2021).

35. Player, T. C. & Hore, P. J. Source of magnetic field effects on the electrocatalytic reduction of CO2. *J. Chem. Phys.* **153**, 84303 (2020).

36. Adalder, A. *et al.* Carbon black supported manganese phthalocyanine: Efficient electrocatalyst for nitrogen reduction to ammonia. *Eng. Reports* **6**, e12705 (2024).

37. Bartolomé, J., Monton, C. & Schuller, I. K. Magnetism of metal phthalocyanines. *Nanosci. Technol.* 221–245 (2014) doi:10.1007/978-3-642-40609-6_9.

38. Barraclough, C. G., Martin, R. L., Mitra, S. & Sherwood, R. C. Paramagnetic Anisotropy, Electronic Structure, and Ferromagnetism in Spin S = 32 Manganese(II) Phthalocyanine. *J. Chem. Phys.* **53**, 1638–1642 (1970).

39. Wang, Z. & Seehra, M. S. Ising-like chain magnetism, Arrhenius magnetic relaxation, and case against 3D magnetic ordering in β-manganese phthalocyanine (C32H16MnN8). *J. Phys. Condens. Matter* **28**, 136002 (2016).

40. Luo, S., Elouarzaki, K. & Xu, Z. J. Electrochemistry in Magnetic Fields. *Angew. Chemie* **134**, e202203564 (2022).

41. Ren, X. *et al.* Spin-polarized oxygen evolution reaction under magnetic field. *Nat. Commun. 2021 121* **12**, 1–12 (2021).

42. Woodward, J. R. Radical Pairs in Solution. *Prog. React. Kinet. Mech.* **27**, 165–207 (2002).

43. Silvi, B. & Savin, A. Classification of chemical bonds based on topological analysis of electron localization functions. *Nat. 1994 3716499* **371**, 683–686 (1994).

44. Hore, P. J. & Mouritsen, H. The Radical-Pair Mechanism of Magnetoreception. *Annu. Rev. Biophys.* **45**, 299–344 (2016).

45. Pan, H. *et al.* Effective Magnetic Field Regulation of the Radical Pair Spin States in Electrocatalytic CO2 Reduction. *J. Phys. Chem. Lett.* **11**, 48–53 (2020).

46. Adalder, A. *et al.* Controlling the Metal-Ligand Coordination Environment of Manganese Phthalocyanine in 1D-2D Heterostructure for Enhancing Nitrate Reduction to Ammonia. *ACS Catal.* 13516–13527 (2023) doi:10.1021/ACSCATAL.3C02747/SUPPL_FILE/CS3C02747_SI_001.PDF.

47. Zhang, B. *et al.* Manganese acting as a high-performance heterogeneous electrocatalyst in carbon dioxide reduction. *Nat. Commun. 2019 101* **10**, 1–8 (2019).

48. Li, J. *et al.* Atomically dispersed manganese catalysts for oxygen reduction in proton-exchange membrane fuel cells. *Nat. Catal. 2018 112* **1**, 935–945 (2018).

49. Yang, Y. *et al.* O-, N-Atoms-Coordinated Mn Cofactors within a Graphene Framework as Bioinspired Oxygen Reduction Reaction Electrocatalysts. *Adv. Mater.* **30**, 1801732 (2018).

50. Sree Raj, K. A., Barman, N., Radhakrishnan, S., Thapa, R. & Rout, C. S. Hierarchical architecture of the metallic VTe2/Ti3C2Tx MXene heterostructure for supercapacitor applications. *J. Mater. Chem. A* **10**, 23590–23602 (2022).

51. Shu, Z. *et al.* High-Throughput Screening of Heterogeneous Transition Metal Dual-Atom Catalysts by Synergistic Effect for Nitrate Reduction to Ammonia. *Adv. Funct. Mater.* **33**, 2301493 (2023).

52. Maintz, S., Deringer, V. L., Tchougréeff, A. L. & Dronskowski, R. LOBSTER: A tool to extract chemical bonding from plane-wave based DFT. *J. Comput. Chem.* **37**, 1030–1035 (2016).

53. Deringer, V. L., Tchougréeff, A. L. & Dronskowski, R. Crystal orbital Hamilton population (COHP) analysis as projected from plane-wave basis sets. *J. Phys. Chem. A* **115**, 5461–5466 (2011).

54. Luo, X., Liang, G., Li, Y., Yu, F. & Zhao, X. Regulating the Electronic Structure of Freestanding Graphene on SiC by Ge/Sn Intercalation: A Theoretical Study. *Molecules* **27**, 9004 (2022).

55. Luo, H. *et al.* Modulating the Active Hydrogen Adsorption on Fe─N Interface for Boosted Electrocatalytic Nitrate Reduction with Ultra-Long Stability. *Adv. Mater.* **35**, 2304695 (2023).

56. Li, J. *et al.* Efficient Ammonia Electrosynthesis from Nitrate on Strained Ruthenium Nanoclusters. *J. Am. Chem. Soc.* **142**, 7036–7046 (2020).

57. Xiang, J. *et al.* Tandem Electrocatalytic Reduction of Nitrite to Ammonia on Rhodium–Copper Single Atom Alloys. *Adv. Funct. Mater.* 2401941 (2024) doi:10.1002/ADFM.202401941.

58. Yao, Y., Zhu, S., Wang, H., Li, H. & Shao, M. A Spectroscopic Study of Electrochemical Nitrogen and Nitrate Reduction on Rhodium Surfaces. *Angew. Chemie Int. Ed.* **59**, 10479–10483 (2020).

59. Pérez-Gallent, E., Figueiredo, M. C., Katsounaros, I. & Koper, M. T. M. Electrocatalytic reduction of Nitrate on Copper single crystals in acidic and alkaline solutions. *Electrochim. Acta* **227**, 77–84 (2017).

60. Kresse, G. & Furthmüller, J. Efficiency of ab-initio total energy calculations for metals and semiconductors using a plane-wave basis set. *Comput. Mater. Sci.* **6**, 15–50 (1996).

61. Perdew, J. P., Burke, K. & Ernzerhof, M. Generalized Gradient Approximation Made Simple. *Phys. Rev. Lett.* **77**, 3865 (1996).

62. Grimme, S. Semiempirical GGA-type density functional constructed with a long-range dispersion correction. *J. Comput. Chem.* **27**, 1787–1799 (2006).